Nanoscale Horizons

COMMUNICATION

# Evidence of a magnetic transition in atomically thin $Cr_2TiC_2T_x$ MXene†

Cite this: DOI: 10.1039/d0nh00343c

Received 8th June 2020,
Accepted 15th October 2020

DOI: 10.1039/d0nh00343c

rsc.li/nanoscale-horizons

Kanit Hantanasirisakul,[ab] Babak Anasori,‡*[ab] Slavomir Nemsak,[c] James L. Hart,§[b] Jiabin Wu,[abd] Yizhou Yang,[b] Rajesh V. Chopdekar,[c] Padraic Shafer,[c] Andrew F. May,[e] Eun Ju Moon,[b] Jun Zhou,[d] Qinghua Zhang,[f] Mitra L. Taheri,§[b] Steven J. May[b] and Yury Gogotsi*[ab]

**Two-dimensional (2D) transition metal carbides and nitrides known as MXenes have shown attractive functionalities such as high electronic conductivity, a wide range of optical properties, versatile transition metal and surface chemistry, and solution processability. Although extensively studied computationally, the magnetic properties of this large family of 2D materials await experimental exploration. 2D magnetic materials have recently attracted significant interest as model systems to understand low-dimensional magnetism and for potential spintronic applications. Here, we report on synthesis of $Cr_2TiC_2T_x$ MXene and a detailed study of its magnetic as well as electronic properties. Using a combination of magnetometry, synchrotron X-ray linear dichroism, and field- and angular-dependent magnetoresistance measurements, we find clear evidence of a magnetic transition in $Cr_2TiC_2T_x$ at approximately 30 K, which is not present in its bulk layered carbide counterpart ($Cr_2TiAlC_2$ MAX phase). This work presents the first experimental evidence of a magnetic transition in a MXene material and provides an exciting opportunity to explore magnetism in this large family of 2D materials.**

### New concepts

MXene is a large and rapidly growing family of 2D transition metal carbides, carbonitrides, and nitrides with outstanding electronic, optoelectronic, mechanical, and thermal properties. Within less than a decade after the first MXene, $Ti_3C_2T_x$, was discovered, more than 30 MXenes with different compositions have been experimentally synthesized. Given the large number of transition metals that can be included in their structure, MXenes have been predicted to form a plethora of 2D magnetic materials. However, their magnetic properties remain largely unexplored experimentally. In this work, we provide an experimental evidence of a magnetic transition in $Cr_2TiC_2T_x$, an ordered double transition metal carbide MXene, using a combination of magnetometry, spectroscopy, and magnetotransport measurements. This finding adds a new functionality to the MXene family and paves the way for further studies of magnetism in this large family of 2D materials. The desired magnetic properties can potentially be achieved by manipulation of the transition metal compositions including solid solutions, C/N ratio, surface terminations, and interlayer magnetic coupling in MXenes. This multi-level control of magnetic properties is a unique advantage of MXenes compared to other existing 2D magnets.

## Introduction

Following the realization of ferromagnetic ordering in monolayer $CrI_3$ and ultrathin $Cr_2Ge_2Te_6$,[1,2] there has been a surge in the discoveries of intrinsic 2D magnetic materials as well as their applications.[3–14] However, most 2D magnetic materials reported to date are produced either by mechanical exfoliation of van der Waals layered materials or sophisticated epitaxial growth on specific substrates.[5,8] In addition, the ultrathin crystals are generally unstable under ambient conditions, so the experiments were either done in inert environments or an additional capping layer was required. This poses a challenge for both fundamental studies and the development of devices using the existing 2D magnetic materials.

Two-dimensional transition metal carbides (MXenes) have received increasing interest in applications including energy storage, optoelectronics, plasmonic, and photonics.[15,16] With several possible combinations of transition metals, a large

[a] A.J. Drexel Nanomaterials Institute, Drexel University, Philadelphia, PA 19104, USA. E-mail: gogotsi@drexel.edu, banasori@iupui.edu
[b] Department of Materials Science and Engineering, Drexel University, Philadelphia, PA 19104, USA
[c] Advanced Light Source, Lawrence Berkeley National Laboratory, Berkeley, CA 94720, USA
[d] Wuhan National Laboratory for Optoelectronics, Huazhong University of Science and Technology, Wuhan 430074, Hubei, P. R. China
[e] Materials Science and Technology Division, Oak Ridge National Laboratory, Oak Ridge, TN 37831, USA
[f] Beijing National Laboratory for Condensed Matter Physics and Institute of Physics, Chinese Academy of Sciences, Beijing 100190, P. R. China

† Electronic supplementary information (ESI) available. See DOI: 10.1039/d0nh00343c

‡ Current address: Mechanical and Energy Engineering, Integrated Nanosystems Development Institute, Purdue School of Engineering and Technology, Indiana University-Purdue University Indianapolis, IN 46202, USA.
§ Current address: Department of Materials Science and Engineering, Johns Hopkins University, Baltimore, MD 21218, USA.

variety of atomic arrangements, and tunable surface chemistry, MXenes exhibit a wide range of electronic and optical properties.[17] Importantly, they can be synthesized *via* solution-processing in large quantity and are relatively stable under ambient conditions compared to other 2D magnets.[18] Although MXenes are an intriguing platform to engineer 2D magnetism due to their large variety of transition metal compositions including Cr and Mn, their magnetic properties remain largely experimentally unexplored. Only a few experimental reports are available for $Ti_3C_2T_x$ ($T_x$ in MXene formulas stands for surface terminations such as =O, –F, –OH, and –Cl), where Pauli paramagnetic behavior was observed after chemical treatments.[19,20] Several density functional theory (DFT) studies have predicted magnetism in several Cr-, V-, Mn-, and Hf-based MXenes.[21–23] Moreover, recent computational efforts focus on magnetic properties of $M''_2M'C_2T_x$ ordered double transition metal MXenes, in which two layers of a transition metal (M″) sandwich a layer of another transition metal (M′) in a MXene 2D flake.[24,25] For example, ferromagnetism has been predicted in $Cr_2VC_2T_x$[26] and $Hf_2VC_2O_2$,[27] with a possibility to tune their magnetic properties by surface modifications, strain, and external electric field.[28] Antiferromagnetism (AFM) has also been predicted for $Cr_2TiC_2T_x$, where the net spin densities reside on the Cr atoms, and the local magnetic moments are ferromagnetically coupled within the same Cr atomic layer and antiferromagnetically coupled with the adjacent Cr layer through the Cr–C bonds.[26] This spin configuration resembles a magnetic tunnel junction, where based on this spin alignment DFT calculations have predicted an out-of-plane magnetoresistance (MR) of up to 400% in $Cr_2TiC_2T_x$,[29] similar to the very large tunneling magnetoresistance recently observed experimentally in few-layer $CrI_3$.[14] Moreover, it has also been predicted that the magnetic properties of $Cr_2TiC_2T_x$ depend strongly on the lattice parameters, surface terminations, and are tunable by external electric field.[26,30] Despite several computational efforts, no experimental reports on the magnetic properties of the 2D $Cr_2TiC_2T_x$ have been available before this study.

Here, we provide direct experimental evidence of a magnetic transition at ~30 K ($T_f$) from a local-moment paramagnet to a state with a collective magnetic response in $Cr_2TiC_2T_x$ MXene, which is produced by scalable solution-processing under ambient conditions (Fig. 1). The magnetic transition is evidenced by a divergence in zero-field-cooled (ZFC) and field-cooled (FC) dc magnetization and a maximum in the ac susceptibility. The transition involves spin freezing to a glassy state, as evidenced by time dependence of the magnetization and frequency dependence of the ac susceptibility. Evidence for a local but not long-range magnetic ground state is inferred from the asymmetric signal observed at the Cr L-edge using temperature-dependent X-ray linear dichroism measurements. We also show that the electronic transport in this MXene is strongly coupled with the magnetic behavior using field- and angular-dependent magnetoresistance measurements. A large negative linear magnetoresistance and a change of angular-dependent magnetoresistance behavior were observed below $T_f$, illustrating that intrinsic magnetism can indeed bring new functionalities to MXenes.

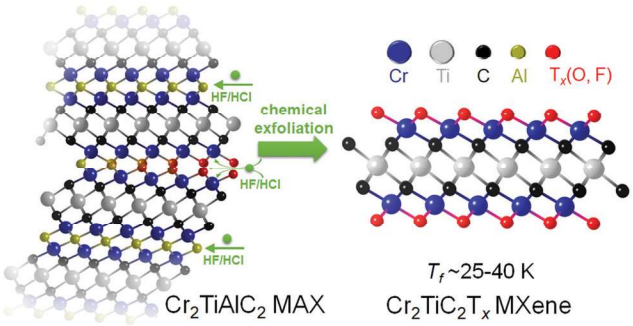


Fig. 1 Synthesis and exfoliation of $Cr_2TiC_2T_x$ MXene. $Cr_2TiC_2T_x$ MXene was synthesized by selective etching of the Al layers from the $Cr_2TiAlC_2$ MAX phase in a mixture of hydrofluoric (HF) and hydrochloric acids (HCl). The resulting multilayer MXene particles were delaminated into atomically thin flakes using tetramethylammonium hydroxide (TMAOH).

## Experimental section

### Synthesis of $Cr_2TiAlC_2$ MAX

$Cr_2TiAlC_2$ was synthesized by mixing Cr, Ti, Al and graphite powders (all from Alfa Aesar, Ward Hill, MA), with mesh sizes of −325, −325, −325 and −300, respectively. The molar ratio of Cr : Ti : Al : C was 2 : 1 : 1.1 : 2. The mixture was ball-milled for 18 h using zirconia milling balls in plastic jars. The powder mixture was placed in an alumina crucible and heated at 5 °C $min^{-1}$ to 1500 °C and held for 1 h under flowing argon. After cooling, the slightly sintered porous compacts were milled into a fine powder using a TiN-coated milling bit. The resulting powder was washed in 9 M HCl acid overnight and sieved through a 400-mesh, producing a powder with a particle size of $<38$ μm.

### Synthesis of $Cr_2TiC_2T_x$ MXene

Typically, 2 g of the $Cr_2TiAlC_2$ MAX powder was etched in a mixture of HF (48–51%, Acros Organics), HCl (37%, Fisher Chemical), and deionized (DI) $H_2O$ with a ratio of 6 : 9 : 15 mL. The reaction mixture was stirred at 35 °C for 42 h. Then the reaction mixture was washed with DI water *via* repeated centrifugation to bring the pH close to neutral. After the washing process, the mixture was filtered on a polypropylene membrane (3501 Coated PP, Celgard LLC Co.) to collect multi-layered (ML-) $Cr_2TiC_2T_x$ MXene. Additional 200 mL of DI water was used to rinse the powder on top of the filtration setup. To delaminate the $Cr_2TiC_2T_x$ MXene, the ML-powder was added to a mixture of 1 : 9 mL of tetramethylammonium hydroxide (TMAOH, 25% in water, Sigma): DI water. The mixture was stirred overnight at room temperature. After that, the mixture was washed with DI water and centrifuged at 10 000 rpm (12 850 rcf) 4–5 times (50 mL of DI water per wash cycle). The reaction mixture was then probe-sonicated (Fisher Scientific model 505 Sonic Dismembrator, 500 W) for 30 min with a 4 s on alternated with 4 s off pulse. The temperature of the vial was kept at −9 °C

 

and argon gas was bubbled through the vial during the sonication process to prevent oxidation of MXene. Finally, the mixture was collected by centrifugation at 3500 rpm for 1 h. The supernatant containing mono- to few-layer flakes of delaminated (d-) $Cr_2TiC_2T_x$ was used for the studies. Note that although centrifugation at 3500 rpm for 1 h has been shown to sufficiently separate mono- to few-layer MXene flakes from other reaction by-products, there might still be a possibility of having nanoparticle by-products that do not sediment after centrifugation. However, we did not observe any nanoparticles in the final d-$Cr_2TiC_2T_x$ solution used in our studies.

Free-standing films of MXene were produced by vacuum-assisted filtration of $\sim$20 mL of the d-$Cr_2TiC_2T_x$ solution with a concentration around 1 mg mL$^{-1}$ over a Celgard membrane. Once all the water was removed from the film, it was further dried in a vacuum oven at room temperature. Prolonged exposure of the film to ambient environment might lead to degradation, which may alter magnetic and electronic properties of the MXene. For annealing, the films were placed on an alumina crucible and heated either to 150 °C in a vacuum oven or to 500 °C in a quartz furnace at 10 °C min$^{-1}$ under 100 mL min$^{-1}$ flow of Ar. The samples were held at the designated annealing temperature for 3 h before cooling down naturally. All processes were done using non-magnetizable labware to ensure that there is no magnetic contamination.

### Materials characterizations

AFM images were obtained using a Bruker AFM Multimode 8 with a standard tapping mode in air. Driving frequency of 299 kHz, driving amplitude of 17 mV, and scanning frequency of 0.3 Hz were used for the measurement. d-$Cr_2TiC_2T_x$ solution was spin-casted on a $Si/SiO_2$ substrate and dried under vacuum before the measurement. SEM images were obtained using a Zeiss Supra 50VP electron microscope operated at 5 kV. EDX spectra was collected using Oxford Inca X-Sight, U.K. attached to the SEM. The spectra were collected on 4 spots of the same sample and the average values are reported. XRD patterns were recorded using MiniFlex X-ray diffractometers using Cu Kα radiation operated at 40 kV and 15 mA. XPS spectra were collected using a Physical Electronics, Versa Probe 5000 spectrometer with a monochromatic Al Kα X-ray source. Charge neutralization was performed using a dual-beam charge neutralizer. High-resolution spectra were collected at a pass energy of 23.5 eV with a step size of 0.05 eV. The peak fitting of the core-level spectra was performed using Casa XPS software package with Shirley-type background. TGA-MS measurement was done using a Discovery SDT 650 thermal balance connected to a Discovery mass spectrometer (TA Instruments, DE). The freestanding MXene films with a mass of $\sim$10 mg were dried in a vacuum desiccator at room temperature, packed in a 90 μL alumina pan, and heated to 1500 °C at a heating rate of 10 °C min$^{-1}$ in He atmosphere (100 mL min$^{-1}$). The furnace was purged with He gas (100 mL min$^{-1}$) for 1 h prior to the experiment. HAADF-STEM images and EELS elemental maps were obtained on an ARM-200CF (JEOL, Tokyo, Japan) operating at 200–300 kV and equipped with double spherical aberration correctors. The resolution of the probe, defined by the objective pre-field, was 78 pm. The $Cr_2TiC_2T_x$ and $Cr_2TiAlC_2$ samples for STEM analysis were prepared by drop-casting methods on the TEM grids.

Resistivity and magnetotransport measurements were performed using a Quantum Design EverCool II Physical Property Measurement System (PPMS). For the $\rho$ *vs.* $T$ measurement, MXene free-standing films dried at room temperature, 150 °C, or 500 °C were wired to a PPMS puck in a 4-point configuration using silver wire and silver paint. The film thicknesses were measured by an electronic micrometer (MDH-25M, Mitutoyo, IL). For MR measurements, the external magnetic field of up to 90 kOe was applied perpendicularly to the sample surface and was swept at 50 Oe s$^{-1}$. Dc and ac magnetization measurements were performed on free-standing films (unless otherwise stated) in a Quantum Design MPMS3 (SQUID magnetometry), while vibrating sample magnetometry (VSM) measurements were performed in a Quantum Design PPMS. The Curie–Weiss equation, $\chi_m = C/(T - \theta)$, was used to model the magnetometry data above $T_f$, where $\chi_m$ is the molar magnetic susceptibility (emu per Oe mol Cr), $C$ is the Curie constant (emu K per Oe mol Cr), and $\theta$ is the Weiss constant (K) and $T$ is temperature (K). The effective magnetic moment ($\mu_{eff}$) is calculated from the Curie constant using $\mu_{eff} = (3k_BC/N_A)^{0.5}$, where $k_B$ and $N_A$ are the Boltzmann constant ($1.38 \times 10^{-23}$ J K$^{-1}$) and Avogadro number ($6.02 \times 10^{23}$ atom per mol), respectively. The angular-dependent magnetoresistance of the $Cr_2TiC_2T_x$ and $Ti_3C_2T_x$ MXenes were measured with a horizontal rotator (Quantum Design) with 4-point and van der Pauw contact configurations. The samples were brought to the desired temperatures for measurement and were allowed to reach thermal equilibrium for at least 15 min. The samples were rotated at 1° s$^{-1}$ from 0° to 360° for at least 3 cycles. The data shown in Fig. 4d was smoothed for clarity. The raw data is shown in Fig. S14 (ESI†). Synchrotron characterization was done using photoemission electron microscopy (PEEM) and X-ray magnetic linear dichroism (XMLD). $Cr_2TiC_2T_x$ flakes were deposited on p-Si substrates from d-$Cr_2TiC_2T_x$ solution by spin-coating at 1000 rpm for 2 min and 3000 rpm for 15 s. PEEM measurements were performed at the PEEM3 endstation, beamline 11.0.1 of the Advanced Light Source. Total energy resolution was better than 300 meV. X-ray spectroscopy measurements were performed at beamline 4.0.2 of the Advanced Light Source, with energy resolution better than 150 meV. Photon energies were scanned over the Cr L-edge using s- and p-polarized light in a grazing incidence geometry of 30°. The difference between the s- and p-polarization intensity is due to the X-ray linear dichroism effect, which stems from both structural and magnetic origins.

## Results and discussion

We begin by discussing the structural and chemical characterization of the MAX and MXene samples used in this study. Aberration-corrected cross-section high-angle annular dark-field scanning transmission electron microscope (HAADF-

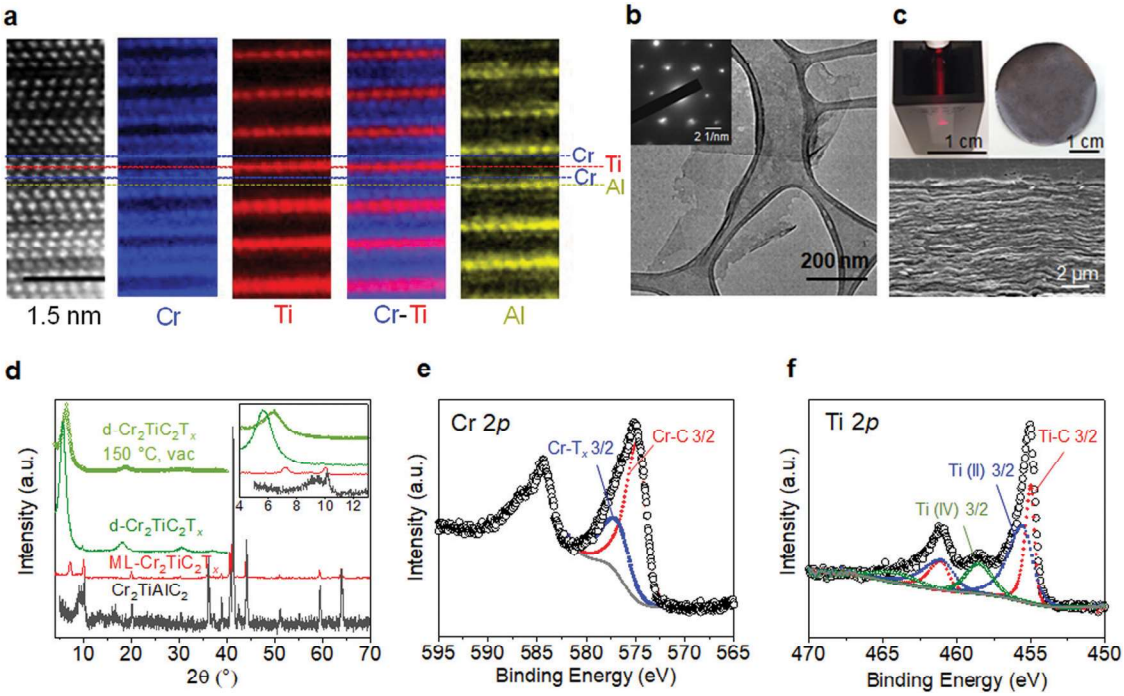


Fig. 2 Structural and chemical characterization of $Cr_2TiAlC_2$ MAX phase and $Cr_2TiC_2T_x$ MXene. (a) Aberration-corrected high-angle annular dark-field scanning transmission electron micrograph and atomic-resolution electron energy loss spectroscopy of $Cr_2TiAlC_2$, indicating that Cr and Ti atoms preferentially occupy the outer and the middle transition metal layers, respectively. (b) Plan-view transmission electron micrograph of 2D $Cr_2TiC_2T_x$ MXene. Inset shows selected-area electron diffraction of the flake. (c) Top left: Optical image of delaminated $Cr_2TiC_2T_x$ MXene colloidal solution. Top right: Optical image of a free-standing film made by vacuum-assisted filtration of the delaminated solution. Bottom: Scanning electron micrograph of the cross-section of the film. (d) XRD patterns of $Cr_2TiAlC_2$ MAX (black), multilayered $Cr_2TiC_2T_x$ MXene (red), and delaminated $Cr_2TiC_2T_x$ (green). Inset shows a zoom-in between $2\theta$ = 4–13°. (e) and (f) Core level XPS spectra of (f) Cr 2p and (g) Ti 2p regions.

STEM) and atomic-resolution electron energy loss spectroscopy (EELS) mapping of the $Cr_2TiAlC_2$ MAX phase shown in Fig. 2a reveal that Cr preferentially occupies the outer transition metal layer, whereas Ti resides in the middle transition metal layer. This is in good agreement with neutron diffraction and density functional theory (DFT) studies reported previously.[31,32] Cross-section transmission electron microscope (TEM) image shown in Fig. S1a, ESI† shows a high quality crystal in a large area without visible atomic defects. Successful conversion of MAX to MXene by selective etching of Al layers and delamination (see Experimental section) is evidenced in the plan-view TEM image (Fig. 2b and Fig. S2, ESI†) and selected-area electron diffraction (SAED, inset of Fig. 2b), showing an atomically thin single crystal $Cr_2TiC_2T_x$ flake with a lateral size around 200–1000 nm, in agreement with the atomic force microscopy image shown in Fig. S1b (ESI†). The delaminated $Cr_2TiC_2T_x$ (d-$Cr_2TiC_2T_x$) solution forms a stable colloidal solution in water, and free-standing films with a thickness of up to 10 μm can be produced by vacuum-assisted filtration of the solution as shown in Fig. 2c.

Although conversion of MAX to MXene with this etching condition was incomplete as revealed by the remaining 002 peak of the MAX phase (at $2\theta$ ~10°) in the X-ray diffraction (XRD) patterns shown in Fig. 2d, delamination and further processing steps (see Experimental section) were employed to ensure that only atomically thin flakes of d-$Cr_2TiC_2T_x$ MXene are present in the samples used for magnetic and electrical measurements. A free-standing film sample shows a sharp 002 peak at 5.7°, corresponding to interlayer spacing of 15.5 Å. The peak shifts to 6.4° (13.8 Å) after vacuum drying at 150 °C due to loss of intercalated water and adsorbed molecules, as observed in other MXenes.[33,34] No other impurity such as oxides or carbides was observed in the XRD patterns of the MXene samples after processing (Fig. 2d and Fig. S1e, ESI†). The absence of oxide nanoparticles was also confirmed by large-area TEM images and SAED pattern shown in Fig. S2 (ESI†).

X-ray photoelectron spectroscopy (XPS) was used to determine atomic ratios of the transition metals as well as to provide insights into their bonding environments. XPS spectrum of the Cr $2p_{3/2}$ (Fig. 2e) can be deconvoluted into two peaks centered at 574.8 eV and 576.8 eV, which are assigned to Cr–C and Cr–$T_x$ bonds, respectively. Although the binding energy of Cr–$T_x$ is in the same range as that of chromium oxides and hydroxides, it can be attributed mainly to the chromium bonded to the oxygen and fluorine surface terminations of MXene since a significant concentration of chromium oxides were not detected in XRD patterns or SAED analysis (see Fig. S1, S2 and Table S1, ESI†). Moreover, $Cr_2O_3$ typically exhibits multiplet peaks at higher binding energies, which were not observed in our samples. For the Ti 2p region (Fig. 2f), the spectrum was fitted by 3 sets of doublets centered at 455.0 eV (461.1 eV), 455.5 eV (461.6 eV), and 458.5 eV (464.1 eV), which correspond to Ti–C, Ti(II), and Ti(IV), respectively (the binding energies in parentheses correspond to Ti $2p_{1/2}$).

 

To study the magnetic properties of the $Cr_2TiC_2T_x$, macroscopic quantities (tens of milligrams) of d-$Cr_2TiC_2T_x$ MXene were synthesized and processed into a textured, free-standing paper (Fig. 2c). The magnetic properties measured from this film morphology inevitably include flake-to-flake coupling, which may affect the macroscopic signal obtained from the magnetometer. The primary characterization was completed by applying the magnetic field ($H$) within the plane of the sample, which is perpendicular to the $c$-axis of $Cr_2TiC_2T_x$, assuming the papers are perfectly textured. The results are summarized in Fig. 3. In Fig. 3a, magnetization data obtained above 50 K from the MXene are compared to the full temperature-dependence of the parent MAX phase ($Cr_2TiAlC_2$); these results demonstrate that solution-based exfoliation to $Cr_2TiC_2T_x$ greatly enhances the magnetization. Above 100 K, the $Cr_2TiC_2T_x$ sample shows a local-moment paramagnetic response that can be well-described using the Curie–Weiss model. For $H$ = 10 kOe, fitting the data between 100 and 350 K yields an effective moment of 2.73 $\mu_B$ per Cr atom and a Weiss temperature ($\theta$) of −30.3 K (red line Fig. 3a). The effective moment is slightly reduced from that expected for $Cr^{3+}$ (3.86 $\mu_B$ per Cr atom) but is fairly similar to that predicted by DFT for this MXene (~2.6 $\mu_B$ per Cr atom).[26] The negative Weiss temperature indicates dominant antiferromagnetic interactions. The parent MAX phase shows only Pauli paramagnetic behavior, where the magnetization is relatively independent of temperature and much smaller than in the exfoliated material. This suggests that conversion of MAX to MXene produces a local moment on Cr in $Cr_2TiC_2T_x$ and illustrates that residuals of the MAX phase cannot account for the observed magnetic transition.

The magnetic transition at $T_f$ ~ 30 K in $Cr_2TiC_2T_x$ is evidenced through a bifurcation of the zero-field-cooled (ZFC) and field-cooled (FC) dc magnetization (Fig. 3b and Fig. S4, ESI†) as well as by a maximum in the ac susceptibility (Fig. 3c). The in-phase component $\chi'$ of the ac susceptibility is shown in Fig. 3c and the small out-of-phase contribution is shown in Fig. S5 (ESI†). $\chi'$ has a slight frequency dependence, suggesting a spin freezing transition to a glassy state. Consistent with this, we found that the bifurcation of the ZFC-FC dc magnetization data is decreased as the applied field increases (Fig. S4a, ESI†). The isothermal magnetizations $M(H)$ are shown in Fig. 3d and e. The small and linear $M(H)$ observed for $Cr_2TiAlC_2$ is expected for this Pauli paramagnetic phase, while the MXene sample has a much larger induced magnetization with strong curvature in $M(H)$ at 5 K (Fig. 3d). Close inspection reveals a remanence (non-zero moment at $H$ = 0) after decreasing the field from 60 kOe. However, this data does not imply ferromagnetic behavior because the net moment is small relative to the effective moment and a time-dependent decay of the remanent magnetization is observed, as shown in Fig. 3f. Similarly, a slow increase in magnetization is observed at 10 K upon applying a magnetic field following an initial zero-field-cooled (Fig. S4b,

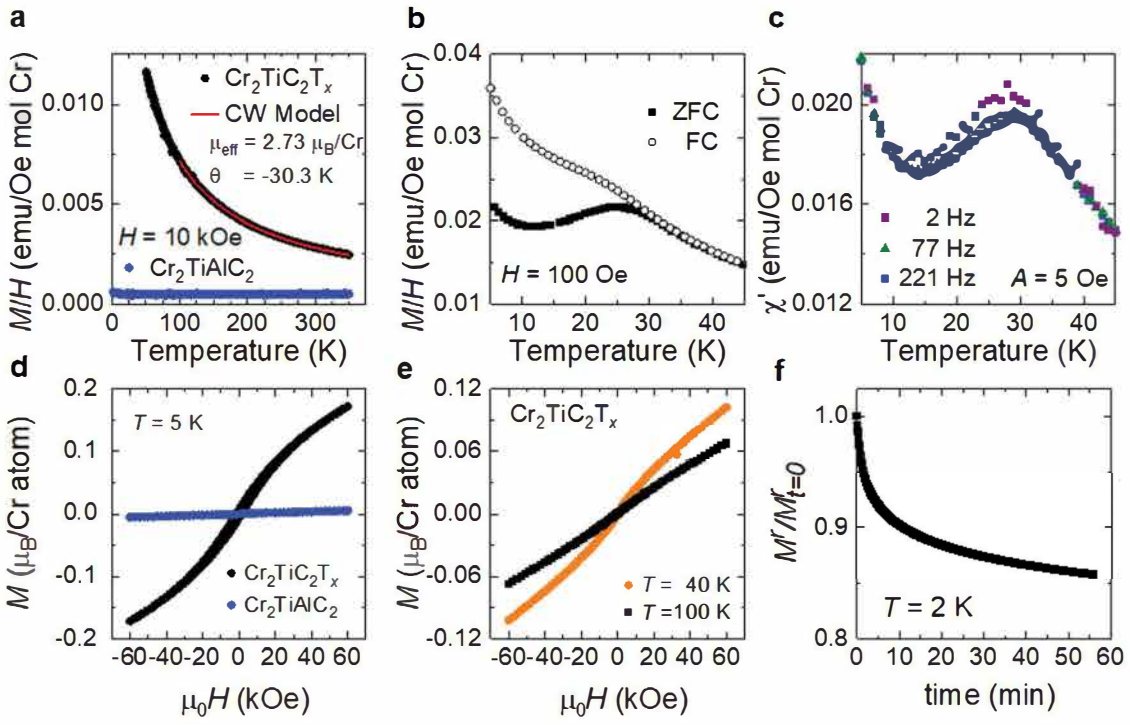


**Fig. 3** Magnetic characterization of $Cr_2TiC_2T_x$ MXene and $Cr_2TiAlC_2$ MAX phase. (a) Field-cooled (FC) magnetization of $Cr_2TiC_2T_x$ MXene (black) and $Cr_2TiAlC_2$ MAX phase (blue) measured using 10 kOe external magnetic field. The data from $Cr_2TiC_2T_x$ was fitted with Curie–Weiss (CW) model. (b) Zero-field-cooled (filled squares) and field-cooled (empty circles) magnetization from 5–45 K of $Cr_2TiC_2T_x$ MXene. (c) In-phase component of ac susceptibility measured at zero dc field with an amplitude of 5 Oe and frequencies ranging from 2–221 Hz. (d) Field-dependent magnetization of $Cr_2TiC_2T_x$ MXene (black) and $Cr_2TiAlC_2$ MAX phase (blue) measured at 5 K. (e) Field-dependent magnetization of $Cr_2TiC_2T_x$ MXene measured at 40 K (orange) and 100 K (black). (f) Time-dependent magnetization measured after cooling $Cr_2TiC_2T_x$ MXene from 300 K to 2 K in 60 kOe external field.

ESI†). All of these features are consistent with $T_f \sim 30$ K being a spin freezing transition to a state with glassy spin dynamics.

The curvature in $M(H)$ at 40 K illustrated in Fig. 3e suggests the strong development of short-range correlations above $T_f$, and a slight curvature in $M(H)$ can be inferred at even 100 K. This can be common in materials undergoing a spin freezing transition when the local interactions are strong but intrinsic disorder prevents long-range magnetic order.[35] First principles calculations of $Cr_2TiC_2T_x$ found that the ground state spin structure depends on $T_x$ with two distinct antiferromagnetic configurations favored for –F and –OH terminations and either ferromagnetic or no magnetic order favored for =O terminations.[26] Thus, the inhomogeneous nature of the surface species inherent to MXenes likely inhibits long-range magnetic order, resulting in a glassy state. Moreover, the magnetic disorder could arise from the flake-to-flake coupling of the randomly oriented flakes inevitably present in the sample studied. Note that a more detailed understanding of the magnetic interactions of this MXene could, in theory, be obtained from measurements on a single flake, however such measurements are challenging given the small magnetization values observed even on free-standing film comprising milligrams of the MXene flakes. At 300 K, both the MAX phase and the MXene show linear $M(H)$, consistent with paramagnetic behavior, as shown in Fig. S6 (ESI†). Magnetization measurements with the applied field perpendicular to the plane of the film were also performed. The magnetic response was found to be somewhat anisotropic, further supporting a bulk phase transition. However, the qualitative $M(T)$ and $M(H)$ are similar for both orientations (see Fig. S5, ESI†). Finally, we note that a Curie tail is observed in the MXene below 10 K, indicating that not all moments are frozen below $T_f$. Subtraction of this contribution to the magnetization, modeled using a Curie–Weiss fit, yields ZFC-FC magnetometry data that is consistent with that typically reported for glassy systems with a nearly temperature-independent FC magnetization and a decreasing ZFC magnetization with decreasing temperature below $T_f$ (Fig. S5f, ESI†).[36,37]

While previous reports of $Cr_2O_3$ nanoparticle have observed a ZFC-FC divergence,[38,39] we do not find any evidence of an oxide secondary phase in the MXene samples as described earlier (Fig. 2 and Fig. S1, S2, ESI†), although the absolute absence of a secondary phase can never be completely ruled out. Moreover, the effective moment obtained from the Curie–Weiss fit (Fig. 3a) was calculated based on the mass of $Cr_2TiC_2T_x$ and the value would have been different by orders of magnitude if the measured magnetization signal was dominated by oxide nanoparticles. We further note that ZFC-FC measurements performed on $Cr_2TiC_2T_x$ multilayer powder and several free-standing films (d-$Cr_2TiC_2T_x$) reproducibly yielded the cusp in the ZFC data within a temperature range from 22 to 27 K for the as-synthesized films and the film annealed at 150 °C, while that of the film annealed at 500 °C was found at 40 K, as shown in Fig. S7 (ESI†). The presence of the magnetic transition in $Cr_2TiC_2T_x$ regardless of the sample preparation or post-synthesis treatments, and the lack of a magnetic transition in the parent MAX powder that often contains secondary Cr-based phases including chromium oxides, further points to the MXene as the origin of the magnetic response.[31] The difference in the transition temperature observed could possibly be due to the difference in surface terminations between different batches of MXene synthesized and surface modification by thermal annealing, which warrants further studies. Moreover, the difference in the flake-to-flake stacking, and thus flake-to-flake coupling and local magnetic interactions, between different samples could also play a role in the variation in the transition temperature and the broad peak in the ZFC curves.

To further investigate the magnetic properties of the free-standing film (d-$Cr_2TiC_2T_x$), we performed X-ray absorption (XA) spectroscopy with orthogonal orientations of linearly polarized X-ray across the Cr L-edge in the temperature range of 12–300 K (Fig. S8a, ESI†). X-ray linear dichroism (XLD) measures anisotropy in the electronic structure of the Cr species, due to the polarization dependence of the XA measurements. The XLD signal is quite strong (peak intensity $\sim 5\%$) and robust across the entire range of measured temperatures. In general, this XLD signal could originate both from an in-plane *vs.* out-of-plane structural anisotropy and from magnetic ordering. We attribute the temperature-independent XLD signal here to structural anisotropy rather than magnetic order because temperature will only weakly affect the structural asymmetry of the MXene in the absence of a structural phase transition. This result highlights the highly 2D nature of the layered MXene structure that is present even in the macroscopic free-standing films, which we also demonstrated by an agreement with XA and XLD measurements of $Cr_2TiC_2T_x$ flakes dispersed on the Si substrate (Fig. S8b, ESI†). The lack of a magnetic contribution to the XLD signal can be explained by the disordered magnetic moments in a relaxed spin glass below the transition temperature $T_f$ and paramagnetic behavior above $T_f$, in agreement with the magnetometry results. To rule out extrinsic magnetic disorder arising from in-plane rotations of the MXene grains within the film and randomly dispersed MXene flakes, we measured spatially resolved XA spectra of individual flakes using soft X-ray photoemission electron microscopy (PEEM), as shown in Fig. S8c and d (ESI†). XA and XLD spectra localized to a single $Cr_2TiC_2T_x$ flake agree qualitatively with the spatially-averaged XA findings from the film. We note that the spectral features of our measured data are distinctly different from that of $Cr_2O_3$ and $CrO_2$, further supporting the absence of such nanoparticles, which were not observed even within chemical imaging capabilities of PEEM measurements (Fig. S8, ESI†).[40,41]

Electronic transport measurements provide additional evidence that a magnetic transition is present in the MXene. As previously detailed, the presence of intercalants and surface termination lead to significant increases in resistivity ($\rho$) when probed *via* macroscopic transport measurements.[42] For this study, we performed *in situ* annealing of the $Cr_2TiC_2T_x$ MXene in vacuum up to 700 °C, where more than two orders of magnitude decrease in resistivity was observed as described

 

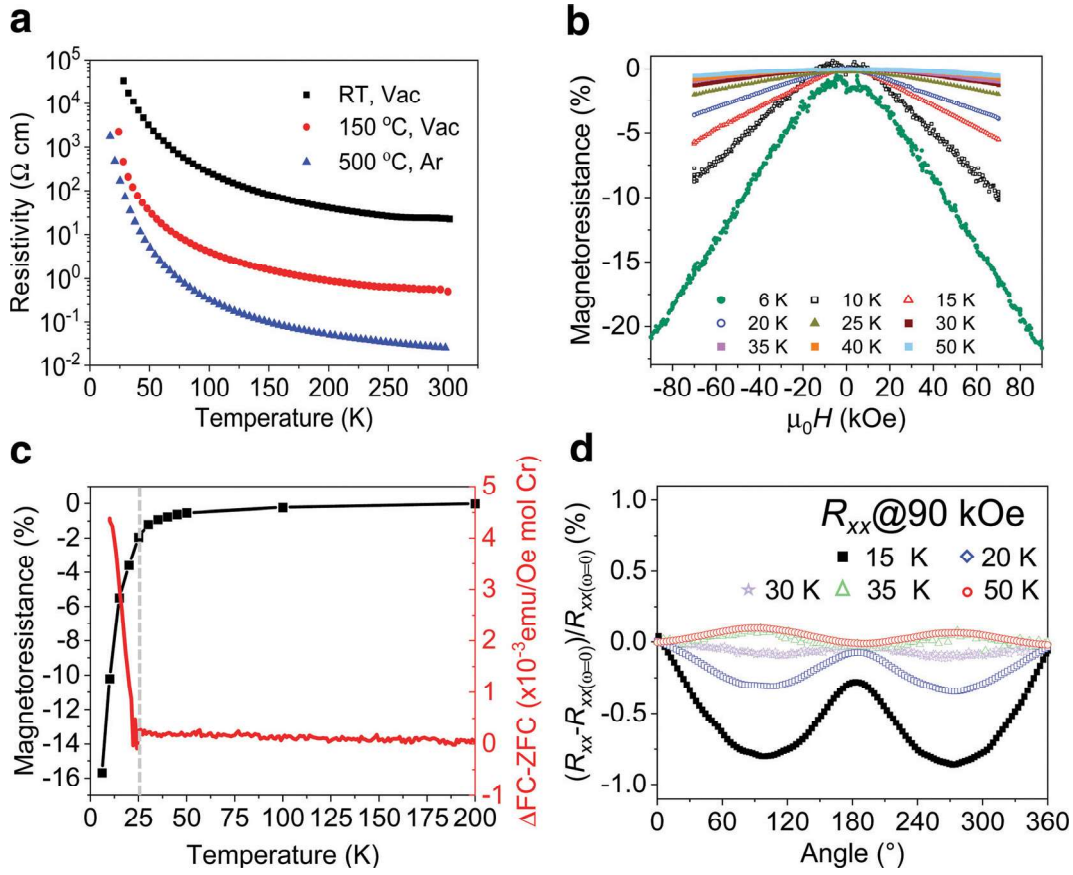


Fig. 4 Magnetotransport measurements. (a) Temperature-dependent resistivity of free-standing films dried at room temperature (black), 150 °C (red), and 500 °C (blue). (b) Field-dependent magnetoresistance of the free-standing film annealed at 150 °C from 6 to 50 K. (c) A comparison between magnitude of magnetoresistance measured at 70 kOe (left axis) and the difference between the field-cooled and zero-field-cooled magnetization (right axis). (d) Angular-dependent longitudinal magnetoresistance ($R_{xx}$) measured at 90 kOe from 15 to 50 K.

in Fig. S9 (ESI†). As suggested by TGA-MS data (Fig. S1e, ESI†), the predominant decrease in resistivity can be attributed to decomposition of $TMA^+$ ions below 500 °C. Therefore, for the low-temperature magnetoresistance measurements, we annealed the d-$Cr_2TiC_2T_x$ MXene free-standing films at either 150 °C or 500 °C to decrease electrical resistivity and improve the precision of the measurements. As shown in Fig. 4a, the magnitude of the resistivity decreases significantly after these anneals, but the slope of temperature-dependent resistivity ($d\rho/dT$) remains negative, consistent with the *in situ* annealing experiment (Fig. S9, ESI†). $Cr_2TiC_2T_x$ shows some of the strongest dependence of resistivity on temperature for MXenes reported so far, where the resistivity increases by a few orders of magnitude upon cooling the samples below 50 K.[15] A sharp increase in the junction resistance was also observed in $CrI_3$ tunnel junction device with a kink near the magnetic transition temperature, which is caused by different barrier heights experienced by electrons with opposite spins.[43] Although we did not observe any anomaly in the temperature-dependence of resistivity, a clear inflection point in the reduced activation energy analysis is observed near 30 K, suggesting a coupling between the electronic transport and magnetic state of the MXene (Fig. S11, ESI†). Note that our macroscopic transport measurement on the MXene free-standing films, comprise stacked of many 2D flakes, may be the reason for low sensitivity of resistive detection of the magnetic transition temperature. Importantly, the ZFC-FC divergence is maintained even after the 500 °C anneal (Fig. S10a, ESI†), indicating that this annealing step to decrease resistivity of the films does not significantly alter the magnetic transition.

We investigated the magnetotransport properties of the $Cr_2TiC_2T_x$ MXene by measuring field-dependent (MR) and angular-dependent magnetoresistance (AMR) of a free-standing film (d-$Cr_2TiC_2T_x$) dried at 150 °C. For the MR experiments, the change in magnetoresistance (%MR) was recorded at various temperatures as the external magnetic field ($H$) was varied perpendicularly to the sample surface as shown in Fig. 4b. We define %MR as $(\rho_H - \rho_{H=0}/\rho_{H=0}) \times 100\%$, where $\rho_H$ and $\rho_{H=0}$ are the resistivities in the presence and absence of $H$, respectively. $Cr_2TiC_2T_x$ starts to exhibit appreciable MR below 50 K, and its magnitude increases significantly below ~30 K, reaching a negative %MR value of ~20% at 6 K and 90 kOe. This large negative %M*R* observed in $Cr_2TiC_2T_x$ is much more pronounced compared to non-magnetic MXenes, where %MR has been reported to be less than 5% at comparable magnetic field and temperature.[44–46] As can be seen in Fig. 4c,

the change of the %MR magnitude coincides almost perfectly with the divergence observed in the ZFC and FC measurements, pointing to a coupling between magnetic and electronic transport properties. One possible explanation of the negative MR arises from a reduction of spin-dependent scattering of carriers.[47] It is very unlikely that impurity oxide particles (if there are any presence in the sample) are accountable for both the peak in ZFC curve and the macroscopic magnetotransport behaviors of the MXene. We note in passing that, in contrast to a classical quadratic magnetoresistance, the MR observed in $Cr_2TiC_2T_x$ is linear above ±20 kOe as shown in Fig. S12 (ESI†). Similar MR behavior was also observed in the sample annealed at 500 °C (Fig. S10, ESI†), suggesting that the magnetotransport behavior is independent of intercalant and/or surface termination.

Angular-dependent magnetoresistance (AMR) measurements, where the longitudinal resistance ($R_{xx}$) and Hall resistance ($R_{xy}$) of a d-$Cr_2TiC_2T_x$ free-standing film are recorded as it is rotated with respect to $H$, provide further evidence of the magnetic transition and coupling between magnetic and electronic transport properties. Here, $H$ is perpendicular (parallel) to the sample surface at 0° (90°), see Fig. S13, ESI† and Experimental Section. We define the normalized AMR as $(R_\omega - R_{\omega=0})/R_{\omega=0} \times 100\%$, where $\omega$ is the angle between the applied field direction and the sample surface; $R_\omega$ and $R_{\omega=0}$ are the resistance values measured at $\omega$ and 0°, respectively. Shown in Fig. 4d are normalized $R_{xx}$ of $Cr_2TiC_2T_x$ measured from 15 to 50 K with $H$ = 90 kOe. Strikingly, $R_{xx}$ shows a clear difference between that measured above and below $T_f$. At 35 and 50 K, $R_{xx}$ exhibits an almost identical functional form analogous to $\sin^2\omega$ with two maxima at around 90° and 270°. However, it changes to a different functional form with two minima at lower temperatures and the magnitude of the minima increases with decreasing temperature. Note that at 35 K and above, the resistance is maximum when $H$ is parallel to the sample surface (90°), while the opposite is true at 30 K and lower temperatures. This suggests the presence of an anisotropic magnetoresistance component, which might stem from anisotropic magnetization of the $Cr_2TiC_2T_x$ below $T_f$. Similar changes in the shape of $R_{xy}$ are observed below 30 K, as presented in Fig. S13 (ESI†). Although the magnetotransport property of MXenes is not well-understood,[48] this abrupt change of the magnetoresistance at the magnetic transition temperature provides further evidence of a coupling between magnetic and magnetoelectronic transport of $Cr_2TiC_2T_x$. For comparison, the paramagnetic $Ti_3C_2T_x$ MXene shows negligible difference in AMR between 10 and 50 K (Fig. S15, ESI†).

## Conclusions

In summary, we presented clear evidence of a magnetic transition in 2D $Cr_2TiC_2T_x$ MXene at ~30 K, which was not observed in its $Cr_2TiAlC_2$ MAX precursor. Magnetometry reveals a clear bifurcation in the macroscopic magnetization as measured under ZFC and FC conditions, along with the presence of glassy dynamics in the low-temperature state. The divergence of the ZFC-FC magnetization is accompanied by a significant increase in magnetoresistance that is negative, linear and non-saturating up to 90 kOe below $T_f$. The demonstration of a magnetic transition in the $Cr_2TiC_2T_x$ demonstrates the feasibility of MXenes to host magnetic interactions and lays the groundwork for future studies of magnetism in this relatively new and rapidly growing family of 2D transition metal carbides and nitrides.

## Conflicts of interest

Q4

## Acknowledgements

This work was funded by the U.S. Department of Energy (DOE), Office of Science, Office of Basic Energy Sciences, grant #DE-SC0018618. XMLD measurements were performed at the PEEM3 end station of beamline 11.0.1 and the VMM end station of beamline 4.0.2 at the Advanced Light Source, the U.S. Department of Energy, Office of Science User Facility under contract no. DE-AC02-05CH11231. J. L. H. and M. L. T. acknowledge funding from the National Science Foundation (NSF) MRI award #DMR-1429661 to support the high temperature resistance measurements performed within a TEM. Magnetic characterization (A. F. M.) was supported by the U. S. Department of Energy, Office of Science, Basic Energy Sciences, Materials Sciences and Engineering Division. Dr Xu Xiao is acknowledged for help with TEM measurements. Prof. Goran Karapetrov is acknowledged for providing access to AFM.

Q5

## References

1 B. Huang, G. Clark, E. Navarro-Moratalla, D. R. Klein, R. Cheng, K. L. Seyler, D. Zhong, E. Schmidgall, M. A. McGuire, D. H. Cobden, W. Yao, D. Xiao, P. Jarillo-Herrero and X. Xu, *Nature*, 2017, **546**, 270.

2 C. Gong, L. Li, Z. Li, H. Ji, A. Stern, Y. Xia, T. Cao, W. Bao, C. Wang, Y. Wang, Z. Q. Qiu, R. J. Cava, S. G. Louie, J. Xia and X. Zhang, *Nature*, 2017, **546**, 265.

3 D. Ghazaryan, M. T. Greenaway, Z. Wang, V. H. Guarochico-Moreira, I. J. Vera-Marun, J. Yin, Y. Liao, S. V. Morozov, O. Kristanovski, A. I. Lichtenstein, M. I. Katsnelson, F. Withers, A. Mishchenko, L. Eaves, A. K. Geim, K. S. Novoselov and A. Misra, *Nat. Electron.*, 2018, **1**, 344.

4 M. Abramchuk, S. Jaszewski, K. R. Metz, G. B. Osterhoudt, Y. Wang, K. S. Burch and F. Tafti, *Adv. Mater.*, 2018, **30**, e1801325.

5 K. S. Burch, D. Mandrus and J. G. Park, *Nature*, 2018, **563**, 47.

6 C. Gong and X. Zhang, *Science*, 2019, **363**, eaav4450.

7 W. Zhang, P. K. J. Wong, R. Zhu and A. T. S. Wee, *InfoMat*, 2019, **1**, 479.

8 H. Li, S. Ruan and Y.-J. Zeng, *Adv. Mater.*, 2019, **31**, 1900065.

 

9 B. Huang, G. Clark, D. R. Klein, D. MacNeill, E. Navarro-Moratalla, K. L. Seyler, N. Wilson, M. A. McGuire, D. H. Cobden, D. Xiao, W. Yao, P. Jarillo-Herrero and X. Xu, *Nat. Nanotechnol.*, 2018, **13**, 544.

10 S. Jiang, L. Li, Z. Wang, K. F. Mak and J. Shan, *Nat. Nanotechnol.*, 2018, **13**, 549.

11 S. Jiang, J. Shan and K. F. Mak, *Nat. Mater.*, 2018, **17**, 406.

12 Y. Deng, Y. Yu, Y. Song, J. Zhang, N. Z. Wang, Z. Sun, Y. Yi, Y. Z. Wu, S. Wu, J. Zhu, J. Wang, X. H. Chen and Y. Zhang, *Nature*, 2018, **563**, 94.

13 T. Song, X. Cai, M. W. Tu, X. Zhang, B. Huang, N. P. Wilson, K. L. Seyler, L. Zhu, T. Taniguchi, K. Watanabe, M. A. McGuire, D. H. Cobden, D. Xiao, W. Yao and X. Xu, *Science*, 2018, **360**, 1214.

14 Z. Wang, I. Gutierrez-Lezama, N. Ubrig, M. Kroner, M. Gibertini, T. Taniguchi, K. Watanabe, A. Imamoglu, E. Giannini and A. F. Morpurgo, *Nat. Commun.*, 2018, **9**, 2516.

15 K. Hantanasirisakul and Y. Gogotsi, *Adv. Mater.*, 2018, **30**, 1804779.

16 H. Kim and H. N. Alshareef, *ACS Mater. Lett.*, 2019, **2**, 55.

17 Y. Gogotsi and B. Anasori, *ACS Nano*, 2019, **13**, 8491.

18 C. J. Zhang, S. Pinilla, N. McEvoy, C. P. Cullen, B. Anasori, E. Long, S.-H. Park, A. Seral-Ascaso, A. Shmeliov, D. Krishnan, C. Morant, X. Liu, G. S. Duesberg, Y. Gogotsi and V. Nicolosi, *Chem. Mater.*, 2017, **29**, 4848.

19 Y. Yoon, T. A. Le, A. P. Tiwari, I. Kim, M. W. Barsoum and H. Lee, *Nanoscale*, 2018, **10**, 22429.

20 B. Scheibe, K. Tadyszak, M. Jarek, N. Michalak, M. Kempiński, M. Lewandowski, B. Peplińska and K. Chybczyńska, *Appl. Surf. Sci.*, 2019, **479**, 216.

21 C. Si, J. Zhou and Z. Sun, *ACS Appl. Mater. Interfaces*, 2015, **7**, 17510.

22 M. Khazaei, M. Arai, T. Sasaki, C. Y. Chung, N. S. Venkataramanan, M. Estili, Y. Sakka and Y. Kawazoe, *Adv. Funct. Mater.*, 2013, **23**, 2185.

23 J. He, P. Lyu and P. Nachtigall, *J. Mater. Chem. C*, 2016, **4**, 11143.

24 B. Anasori, Y. Xie, M. Beidaghi, J. Lu, B. C. Hosler, L. Hultman, P. R. Kent, Y. Gogotsi and M. W. Barsoum, *ACS Nano*, 2015, **9**, 9507.

25 B. Anasori, C. Shi, E. J. Moon, Y. Xie, C. A. Voigt, P. R. C. Kent, S. J. May, S. J. L. Billinge, M. W. Barsoum and Y. Gogotsi, *Nanoscale Horiz.*, 2016, **1**, 227.

26 J. Yang, X. Zhou, X. Luo, S. Zhang and L. Chen, *Appl. Phys. Lett.*, 2016, **109**, 203109.

27 L. Dong, H. Kumar, B. Anasori, Y. Gogotsi and V. B. Shenoy, *J. Phys. Chem. Lett.*, 2017, **8**, 422.

28 N. C. Frey, A. Bandyopadhyay, H. Kumar, B. Anasori, Y. Gogotsi and V. B. Shenoy, *ACS Nano*, 2019, **13**, 2831.

29 J. Yang, S. Zhang, A. Wang, R. Wang, C. K. Wang, G. P. Zhang and L. Chen, *Nanoscale*, 2018, **10**, 19492.

30 J. He, G. Ding, C. Zhong, S. Li, D. Li and G. Zhang, *Nanoscale*, 2018, **11**, 356.

31 Z. Liu, E. Wu, J. Wang, Y. Qian, H. Xiang, X. Li, Q. Jin, G. Sun, X. Chen, J. Wang and M. Li, *Acta Mater.*, 2014, **73**, 186.

32 P. A. Burr, D. Horlait and W. E. Lee, *Mater. Res. Lett.*, 2017, **5**, 144.

33 K. Hantanasirisakul, M. Alhabeb, A. Lipatov, K. Maleski, B. Anasori, P. Salles, C. Ieosakulrat, P. Pakawatpanurut, A. Sinitskii, S. J. May and Y. Gogotsi, *Chem. Mater.*, 2019, **31**, 2941.

34 M. Alhabeb, K. Maleski, B. Anasori, P. Lelyukh, L. Clark, S. Sin and Y. Gogotsi, *Chem. Mater.*, 2017, **29**, 7633.

35 N. Roth, F. Ye, A. F. May, B. C. Chakoumakos and B. B. Iversen, *Phys. Rev. B: Condens. Matter Mater. Phys.*, 2019, **100**, 144404.

36 G. Parisi, *Proc. Natl. Acad. Sci. U. S. A.*, 2006, **103**, 7948.

37 K. Binder and A. P. Young, *Rev. Mod. Phys.*, 1986, **58**, 801.

38 S. A. Makhlouf, *J. Magn. Magn. Mater.*, 2004, **1530**, 272.

39 Z. Yang, J. Zhang, D. Gao, Z. Zhu, G. Yang and D. Xue, *RSC Adv.*, 2015, **5**, 46705.

40 Yu. S. Dedkov, A. S. Vinogradov, M. Fonin, C. König, D. V. Vyalikh, A. B. Preobrajenski, S. A. Krasnikov, E. Yu. Kleimenov, M. A. Nesterov, U. Rüdiger, S. L. Molodtsov and G. Güntherodt, *Phys. Rev. B: Condens. Matter Mater. Phys.*, 2005, **72**, 060401(R).

41 E. N. Yitamben, T. C. Lovejoy, A. B. Pakhomov, S. M. Heald, E. Negusse, D. Arena, F. S. Ohuchi and M. A. Olmstead, *Phys. Rev. B: Condens. Matter Mater. Phys.*, 2011, **83**, 045203.

42 J. L. Hart, K. Hantanasirisakul, A. C. Lang, B. Anasori, D. Pinto, Y. Pivak, J. T. van Omme, S. J. May, Y. Gogotsi and M. L. Taheri, *Nat. Commun.*, 2019, **10**, 522.

43 D. R. Klein, D. MacNeill, J. L. Lado, D. Soriano, E. Navarro-Moratalla, K. Watanabe, T. Taniguchi, S. Manni, P. Canfield, J. Fernández-Rossier and P. Jarillo-Herrero, *Science*, 2018, **360**, 1218.

44 J. Halim, M. R. Lukatskaya, K. M. Cook, J. Lu, C. R. Smith, L. Näslund, S. J. May, L. Hultman, Y. Gogotsi, P. Eklund and M. W. Barsoum, *Chem. Mater.*, 2014, **26**, 2374.

45 J. Halim, E. J. Moon, P. Eklund, J. Rosen, M. W. Barsoum and T. Ouisse, *Phys. Rev. B*, 2018, **98**, 104202.

46 J. Halim, I. Persson, E. J. Moon, P. Kühne, V. Darakchieva, P. O. Å. Persson, P. Eklund, J. Rosen and M. W. Barsoum, *J. Phys.: Condens. Matter*, 2019, **31**, 165301.

47 G. A. Prinz, *Science*, 1999, **283**, 330.

48 T. Ouisse and M. Barsoum, *Mater. Res. Lett.*, 2017, **5**, 365.